

Dispersion of the nonlinear optical susceptibility tensor in centrosymmetric media*

M. D. Levenson[†] and N. Bloembergen

Gordon McKay Laboratory, Harvard University, Cambridge, Massachusetts 02138

(Received 3 July 1974)

The production of light at the combination frequency $2\omega_1 - \omega_2$ in centrosymmetric media has been observed as a function of the frequencies ω_1 and ω_2 and the polarization directions of two incident dye-laser beams. The interference of the Raman resonance with the complex electronic contribution to $\chi^{(3)}$ has been observed. In diamond and in benzene all of the components of the third-order nonlinear susceptibility have been measured and calibrated with respect to known cross sections for spontaneous Raman emission. Contributions to the cubic nonlinearity have also been measured in the fluoride series CaF_2 , SrF_2 , CdF_2 , BaF_2 , and in calcite.

I. INTRODUCTION

In centrosymmetric materials the dominant nonlinear optical processes may be described by terms in the electric polarization which are a cubic function of the electric field amplitudes. The third-order nonlinear susceptibility is, in general, a complex quantity, and is capable of describing the interference between various resonant and nonresonant processes.¹ The first comprehensive study of nonlinear processes in centrosymmetric materials was carried out by Maker and Terhune.² Among other phenomena, they observed the generation of the combination frequency $2\omega_1 - \omega_2$ by two light beams with frequencies ω_1 and ω_2 , respectively. The i th Cartesian component of the polarization is written in terms of the third-order susceptibility term:

$$P_i(2\omega_1 - \omega_2) = \sum_{jkl} \chi_{ijkl}^{(3)}(-2\omega_1 + \omega_2, \omega_1, \omega_1, -\omega_2) \times E_j(\omega_1)E_k(\omega_1)E_l(-\omega_2). \quad (1)$$

Maker and Terhune emphasized that this susceptibility has contributions from the nonresonant electronic processes, from stimulated Raman-scattering processes when the difference frequency $\omega_1 - \omega_2$ corresponds to a Raman-active response, or from two-photon absorption when $2\omega_1$ corresponds to the energy difference between electronic states with the same parity. The processes are schematically depicted in Fig. 1. Although Maker and Terhune looked for an interference between the nonresonant term and the Raman effect, the early experimental technique at their disposal did not permit its detection.

Since the real part of the Raman susceptibility is positive for $\omega_1 - \omega_2 - \omega_{\text{vib}} < 0$ but negative for $\omega_1 - \omega_2 - \omega_{\text{vib}} > 0$, the observed intensity $I(2\omega_1 - \omega_2)$, proportional to $|\chi^{(3)}|^2$, should show a minimum on the high-frequency side, when $\omega_1 - \omega_2$ is tuned through the Raman resonance. At this minimum the real part of the Raman susceptibility, partially

or completely, cancels the nonresonant nonlinearity.

This effect was first observed by frequency-mixing experiments³ with CO_2 -laser beams in n -type InSb. In this case the Raman scattering occurred from orbital Landau levels, and $\omega_{\text{vib}} = g\mu_B H_0 \hbar^{-1}$, could be tuned continuously by varying the external field. The effect has subsequently also been observed and discussed theoretically for spin-flip Raman lasers.⁴

The availability of tunable pulsed dye lasers has made it possible to extend the original experiments of Maker and Terhune, with much improved precision and sensitivity, over a wide range of frequencies to a variety of centrosymmetric materials. A very sharp antiresonance has been demonstrated in diamond by this technique.⁵ The interference of the nonresonant nonlinearity with Raman resonance and two photon absorption processes has also been demonstrated in liquids containing benzene.⁶

The situation in noncentrosymmetric crystals is

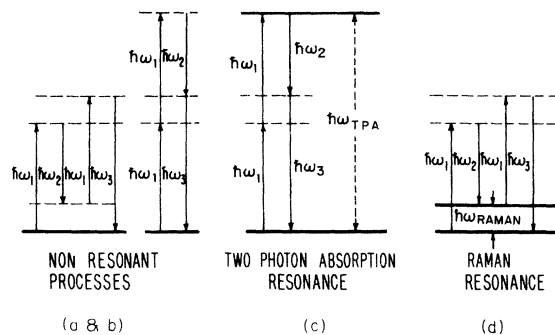


FIG. 1. Four photon parametric processes contributing to the three-wave-mixing signal. Dashed lines denote virtual levels whereas the solid lines stand for real energy states. The processes diagrammed in (a) and (b) give rise to the nonresonant susceptibility while (c) and (d) contribute the resonant-Raman and two-photon-absorbing terms, respectively.

more complicated because in this case interference terms between $\chi^{(3)}$ and two-step processes proportional to $\{\chi^{(2)}\}^2$ also exist. A comprehensive theory of all the dispersive effects has been developed by Flytzanis.⁷ Some experimental results in noncentrosymmetric materials exhibiting interference effects between different nonlinear processes have been reported.⁸⁻¹⁰

It is the purpose of this paper to show how a systematic study of the dispersion characteristics of $I(2\omega_1 - \omega_2)$ in centrosymmetric cubic crystals and liquids permits an accurate determination of the complete susceptibility tensor in terms of one or two known Raman cross sections. Two-photon absorption cross sections can also be calibrated in terms of the reference, and a meaningful test of Kleinman's relation and other approximate models is possible.

In Sec. II the theoretical information, which is based directly on the work by Maker and Terhune, will be summarized. Section III describes the experimental equipment and the techniques of data reduction. Section IV presents the experimental results and the conclusion that may be drawn from them.

II. THEORETICAL REVIEW OF THE DISPERSION IN THREE-WAVE-LIGHT MIXING

Explicit and comprehensive quantum-mechanical analyses are too cumbersome for a direct evaluation of specific experimental data.¹¹ In this section attention will be focused on the three types of processes that dominate the dispersive behavior of a creation of intensity at the frequency $\omega_3 = 2\omega_1 - \omega_2$, when all three frequencies ω_1 , ω_2 , and ω_3 lie in a transparent region of the medium. This dispersion is dominated by dissipative processes at frequencies $2\omega_1$ and $\omega_1 - \omega_2$. The three processes are represented in Fig. 1, and each one possesses its own characteristic symmetry properties. Their relative contributions to different elements of the tensor $\chi^{(3)}$ vary widely.

A. Nonresonant terms

The nonresonant electronic contribution $\chi^{(3)NR}$ results entirely from virtual processes as shown in Figs. 1(a) and 1(b). By definition $\chi^{(3)NR}$ is real, but not necessarily constant. Energy denominators occurring in the perturbation series expansion of the electronic response function result in an undramatic variation of $\chi^{(3)NR}$ with incident frequency similar to the familiar dispersion of the linear dielectric constant. For photon energies much less than the energy of any electronic absorption, one might expect the most strongly varying nonresonant term to make a contribution proportional to

$$\left(\frac{1}{E_- - \hbar\omega}\right)^2 \frac{1}{E_+ - 2\hbar\omega}, \quad (2)$$

where E_- is the average energy difference of electronic states connected by a single-photon transition, and E_+ the average energy difference of states connected by a two-photon absorption.¹¹

Various models and phenomenological rules have been employed to calculate the sign and magnitude of $\chi^{(3)NR}$. Many presuppose more detailed information about the electronic wave functions than is readily available.¹²⁻¹⁴ In our opinion such models describe only qualitative global trends. Since $\chi^{(3)NR}$ contains many terms with different energy denominators and electric dipole matrix elements occur to the fourth power in the numerators, it is clear that simple scaling laws in terms of products of the linear indices refraction at ω_1 , ω_2 , and ω_3 are at best a crude approximation. They may give the correct order of magnitude, but are unable to predict details of the frequency dispersion and anisotropy of the $\chi^{(3)}$ tensor. In this paper $\chi^{(3)NR}$ will be considered as a parameter which must be determined experimentally. The experimental data may then be used to gauge the reliability of various models.

The inadequacy of models becomes obvious, when resonant features at $2\omega_1$ and $\omega_1 - \omega_2$ are taken into account. The models were, of course, never intended to cover such situations, but the diagrams in Fig. 1 and Eq. (2) show that there is a continuous transition between the resonant and nonresonant contributions. The models cannot be "doctored" by including the behavior of the linear index of refraction at $2\omega_1$ and $\omega_1 - \omega_2$, because the two-photon and Raman resonances occur between states with the same parity.

B. Two-photon-absorption terms

The two-photon-absorption processes contribute a complex term to the nonlinear susceptibility, which may be written in the form

$$\chi_{ijhi}^{(3)T}(-\omega_3, \omega_1, \omega_1, -\omega_2) = \sum_m \frac{N_m \alpha_{jhm}^T \alpha_{ilm}^T / 24\hbar}{\omega_m - 2\omega_1 + i\Gamma_m}, \quad (3)$$

where the matrix element $\alpha_{ij,m}^T$ is given by

$$\alpha_{ij,m}^T \equiv \frac{e^2}{\hbar} \left(\frac{n^2 + 1}{3}\right)^2 \times \sum_b \left(\frac{\langle g | x_i | b \rangle \langle b | x_j | m \rangle}{\omega_b + \omega_i} + \frac{\langle g | x_j | b \rangle \langle b | x_i | m \rangle}{\omega_b + \omega_j} \right), \quad (4)$$

where g and m refer to the ground and resonant states and $\hbar\omega_b$ is the energy of the intermediate state b . In Fig. (3), N_m is the density of centers with resonant frequencies ω_m and width Γ_m . The two-photon-absorption constant can be defined analogously to the nonlinear index of refraction²:

$$\gamma^T = -48\pi^2 \text{Im}(\chi^{(3)T}) / n\lambda. \quad (5)$$

If $\chi^{(3)T}$ does not vary appreciably over the frequency range of a given experiment, the two-photon-absorption contribution may be added to the nonresonant term to yield the total complex electronic nonlinearity:

$$\chi^{(3)E} = \chi^{(3)NR} + \chi^{(3)T} = \chi^{(3)E'} - i\chi^{(3)E''}. \quad (6)$$

C. Raman terms

The primary dispersion in the susceptibility $\chi^{(3)}(-\omega_3, \omega_1, \omega_1, -\omega_2)$ observed in our experiments results from vibrational modes of the nuclei with resonant frequencies near $\omega_1 - \omega_2$. Figure 1(d) diagrams the energy levels involved in the process whereby Raman-active vibrational modes produce a third-order polarization at ω_3 . Dispersion due to Raman modes is now sufficiently well understood to serve as a kind of internal reference against which other nonlinear processes are calibrated.

The first-order Raman contribution to the nonlinear susceptibility may be written as

$$\chi_{ijkl}^{(3)R}(-\omega_3, \omega_1, \omega_1, -\omega_2) = \frac{N}{12\hbar} \sum_{\sigma} \frac{\omega_{\sigma} (\alpha_{ij,\sigma}^R \alpha_{kl,\sigma}^R + \alpha_{il,\sigma}^R \alpha_{kj,\sigma}^R)}{\omega_{\sigma}^2 - (\omega_1 - \omega_2)^2 + 2i(\omega_1 - \omega_2)\Gamma_{\sigma}}. \quad (7)$$

Here N is the number of vibrational oscillators per unit volume and ω_{σ} is the vibrational resonant frequency of the mode σ . The local-field-corrected polarizability matrix elements $\alpha_{ij,\sigma}^R$ are defined in terms of the derivative of the linear polarizability with respect to the vibrational normal coordinate:

$$\alpha_{ij,\sigma}^R \equiv \left(\frac{n^2 + 1}{3} \right)^2 \left(\frac{2M\omega}{\hbar} \sigma \right)^{1/2} \left(\frac{d\alpha_{ij}}{dQ_{\sigma}} \right). \quad (8)$$

Combinational factors arising from the permutation symmetry of degenerate fields have been collected in the numerical factor $\frac{1}{12}$. Equations (7) and (8) are a generalization of the formalism used by Maker and Terhune; other authors have written the Raman contribution directly in terms of $d\alpha_{ij}/dQ_{\sigma}$, occasionally absorbing the reduced mass M into the definition of the normal coordinate.^{2,5,7-9}

The total spontaneous Raman-scattering cross section is proportional to the same constant $\sum_{\sigma} |\alpha_{ij,\sigma}^R|^2$, where i denotes the polarization direction of the incident light at ω_1 , and j denotes the polarization direction of the Stokes light at ω_2 . Thus in certain cases $\chi^{(3)R}$ may be considered as a known quantity.

The total third-order polarizability is the sum of the electronic and Raman contributions. Neglecting all but one Raman mode, the general expression is

$$\chi_{ijkl}^{(3)}(-\omega_3, \omega_1, \omega_1, -\omega_2) = \chi_{ijkl}^{(3)E'} - i\chi_{ijkl}^{(3)E''}$$

$$+ \frac{1}{24\hbar} \frac{N(\alpha_{ij,\sigma}^R \alpha_{kl,\sigma}^R + \alpha_{il,\sigma}^R \alpha_{kj,\sigma}^R)}{\omega_{\sigma} - (\omega_1 - \omega_2) + i\Gamma_{\sigma}}. \quad (9)$$

For given polarizations of the incident fields, the nonlinear polarization at frequency ω_3 is proportional to a linear combination of the elements of $\chi_{ijkl}^{(3)}$. The polarization, however, can always be decomposed into a nonresonant complex electronic polarization and a Raman term with resonant behavior.

D. Spatial symmetry

The nonlinear susceptibility is a fourth-rank tensor with elements $\chi_{ijkl}^{(3)}(-\omega_3, \omega_1, \omega_1, -\omega_2)$ where the order of the indices and the corresponding frequencies is to be observed. In our case, there are three distinguishable frequencies. The same convention and notation will be used as adopted by Maker and Terhune,² except that they wrote C instead of $\chi^{(3)}$.

In a medium of cubic symmetry there are three independent tensor components $\chi_{1111}^{(3)}(-\omega_3, \omega_1, \omega_1, -\omega_2)$, $\chi_{1221}^{(3)}(-\omega_3, \omega_1, \omega_1, -\omega_2)$, and $\chi_{1122}^{(3)}(-\omega_3, \omega_1, \omega_1, -\omega_2)$, where 1 and 2 stand for two distinguishable Cartesian directions, e.g., \hat{x} and \hat{y} , which are chosen parallel to the cubic axes.

It is assumed that the two-photon-absorption processes, even if produced by impurities, have the same over-all symmetry. It is also assumed that the \vec{k} vector of the Raman-active vibration is sufficiently small, so that the Raman susceptibility also displays the over-all symmetry of the whole crystal.

In isotropic materials, such as liquids, there are only two independent constants, since the complex susceptibility satisfies the isotropy condition

$$2\chi_{1122}^{(3)} = \chi_{1111}^{(3)} - \chi_{1221}^{(3)}. \quad (10)$$

It is instructive to consider explicitly the symmetry of the Raman vibrations in the cubic crystals used in the present study, diamond and CaF_2 and the other homologous fluorides. In these materials there is one triply degenerate Raman-active vibration with symmetry F_{2g} . This means that the only nonvanishing element is $\alpha_{12,3}^R(\omega_1, -\omega_2, -\omega_1 + \omega_2)$. Contraction on the Cartesian index 3 shows according to Eq. (7) that the Raman contribution to the term of

$$\chi_{1111}^{(3)R} = 0$$

for diamond and the fluorides. In contrast, the symmetry of the Raman mode in liquid benzene at 992 cm^{-1} is nearly totally symmetry (A type); $\langle \alpha_{11,A}^R \rangle^2 \gg \langle \alpha_{12,A}^R \rangle^2$, where the brackets denote an average over molecular orientations. When the polarizations of the fields $E(\omega_1)$ and $E(\omega_2)$ are orthogonal, the vibration is minimally excited. Thus for a totally symmetric mode (zero depolarization)

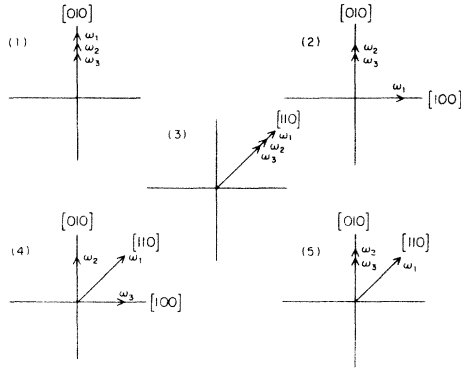


FIG. 2. Five polarization conditions used for cubic and isotropic materials. The axes denote the [100] directions in the cubic crystals and are irrelevant to discussions of isotropic media. The arrows show the directions of the incident electric fields at ω_1 and ω_2 and the source polarization at ω_3 .

$$\chi_{1221}^{(3)R}(-\omega_3, \omega_1, \omega_1, -\omega_2) = 0$$

and

$$\chi_{1111}^{(3)R} = 2\chi_{1122}^{(3)R}.$$

The Raman cross sections for diamond and benzene have been measured with sufficient accuracy that they may be used as calibration references for the determination of the components of $\chi^{(3)}$. The $\chi^{(3)}$ in other materials, such as the fluorides where the Raman cross section is not sufficiently well known, may be determined by using a composite sample, in which the production of light $2\omega_1 - \omega_2$ due to nonresonant parts of the $\chi^{(3)}$ in the unknown material undergoes interferences with the resonant Raman contribution of a material such as benzene in which $\chi^{(3)R}$ is known.

Vibrational modes with resonant frequencies far from the values of $\omega_1 - \omega_2$ used in these experiments, usually make a negligible contribution to the nonresonant susceptibility.

When only one Raman mode of known symmetry

is contributing to the observed resonance, it is possible to cast the observed signal intensity, normalized to unity off resonance, in a form useful for evaluation in cubic and isotropic materials,

$$\frac{I(2\omega_1 - \omega_2)}{I^2(\omega_1)I(\omega_2)} \propto \left| 1 - i \frac{\chi_{\text{eff}}''}{\chi_{\text{eff}}'} + \frac{N|\alpha^R|^2/4\hbar\chi_{\text{eff}}'}{\omega_\sigma - (\omega_1 - \omega_2) + i\Gamma} \right|^2, \quad (11)$$

where

$$\chi_{\text{eff}} = d_1\chi_{1111}^{(3)E} + d_2\chi_{1221}^{(3)E} + d_3\chi_{1122}^{(3)E}. \quad (12)$$

The coefficients d_1 , d_2 , and d_3 depend on the directions of polarization of the two incident light beams and the symmetry of the Raman mode. We have used five different geometries for the incident polarizations, and the observed polarization at $2\omega_1 - \omega_2$. These are schematically shown in Fig. 2. The corresponding values of d_1 , d_2 , and d_3 for each of these polarization conditions are tabulated in Table I for diamond, the fluorides and benzene.

The isotropy condition in Eq. (10) can be used to eliminate one of the susceptibility components of benzene from the expression for the generated intensity in any given polarization condition. Thus only d_1 and d_2 need to be tabulated. The value of d_2 for the polarization geometry (2) must be treated as an unknown parameter since it depends sensitively upon the depolarization ratio ρ for the Raman mode. Were the vibration strictly symmetrical, no Raman contribution would be observed in this geometry and d_2 would be formally infinite.⁶ In diamond, no resonance occurs in geometry (1); d_1 is thus infinite in this case.

These results will be used for the evaluation of the experimental data. They allow a complete determination, with internal consistency checks, of the electronic nonlinear susceptibility tensor elements. This will permit an explicit check on the accuracy of the Kleinman symmetry conjecture for $\chi^{(3)E}$ which would require¹⁵

$$\chi_{1221}^{(3)NR}(-\omega_3, \omega_1, \omega_1, -\omega_2) = \chi_{1122}^{(3)NR}(-\omega_3, \omega_1, \omega_1, -\omega_2).$$

It is clear that this condition does not hold at all for the resonant Raman contribution; small devia-

TABLE I. Nonlinear polarizations and combinatorial factors.

Polarization condition	$P^{NL}/E^2(\omega_1)E(\omega_2)$	Benzene		Diamond		
		d_1	d_2	d_1	d_2	d_3
1	$3\chi_{1111}^{(3)}$	3	0	∞^a	0^a	0^a
2	$3\chi_{1221}^{(3)}$	0	$3\rho^{-1b}$	0	6	0
3	$\frac{1}{2}(3\chi_{1111}^{(3)} + 6\chi_{1122}^{(3)} + 3\chi_{1221}^{(3)})$	3	0	3	3	6
4	$3\chi_{1122}^{(3)}$	3	-3	0	0	12
5	$\frac{1}{2}(3\chi_{1111}^{(3)} + 3\chi_{1221}^{(3)})$	3	3	6	6	0

^aNo Raman resonance.

^b ρ is depolarization ratio of benzene Raman line.

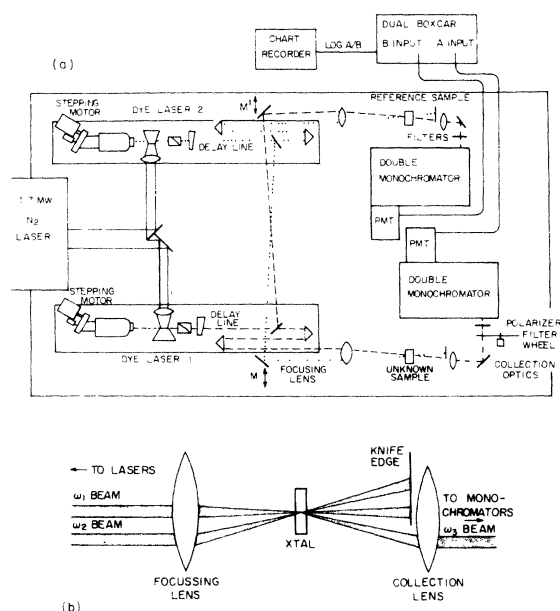


FIG. 3. (a) Experimental equipment employed in optical-mixing spectroscopy. The transversely moveable mirrors at M and M' allow independent adjustments of the crossing angle (and thus coherence length) in each arm of the experiment. (b) Detail of the sample region. Two laser beams are incident upon the crystal, and a third wave is generated by the cubic nonlinearity. The laser beams transmitted through the crystal are blocked, and the third wave is collected and imaged on the monochromator slit.

tions from this condition may be expected in the electronic nonlinearity due to the contribution from two-photon-absorption processes.

Some results on one crystal of trigonal symmetry, calcite, will also be reported. No complete determination of $\chi^{(3)E}$ has been attempted. The number of independent tensor elements would be nine in this case. With Kleinman symmetry this number would be reduced to four.

III. EXPERIMENTAL METHOD

A. Experimental equipment and procedure

Figure 3 diagrams the equipment used in this investigation. The two Hansch-type dye lasers were transversely pumped by the 3371-Å output of a Molectron U. V. -1000 nitrogen laser.¹⁶ The nitrogen laser produced 8-nsec-length pulses of 1-MW peak power roughly ten times a second.

In order to obtain sufficiently narrow spectral output from the dye laser, 40-power Oriol Galilean telescopes were inserted between the gain cells and the gratings. Since the focusing adjustment of the telescopes was critical, they were modified to include spring-loaded micrometers. High quality

plane diffraction gratings selected the desired frequency and directed light of that wavelength back through the telescope to the gain cell. Best results were obtained with Bausch and Lomb 600 line/mm echelette gratings blazed at 2.5 μm . Since roughly 6000 lines were illuminated, the resolution obtained in fifth order was 30 000. The gratings were held in gimbaled mounts equipped with 20:1 reduction differential screw micrometers. To scan frequency $\omega_1 - \omega_2$, both gratings were rotated around a vertical axis by a synchronized mechanical drive.

The light reflected from the grating and re-focused into the dye cell by the telescope was amplified in the gain medium and passed through a rotatable air spaced Glan-Thompson prism for polarization selection. The output mirror of the laser consisted of a highly wedged piece of plate glass. The 4% Fresnel reflection from the first surface provided feedback to the laser cavity; the reflection from the back surface was directed elsewhere to prevent spurious frequency structure in the output.

While the transverse mode structure of the 4-nsec-long 40-kW dye-laser pulses was nearly diffraction limited and quite acceptable, the frequency spectrum showed three undesirable features. For the bulk of the experiment the lasers were equipped with 1200 lines/mm first-order gratings and the output linewidth was 0.8 cm^{-1} . This contributed an instrumental broadening to the traces of the narrowest Raman lines. Second, the output showed broad wings which fell off as $1/(\omega - \omega_L)$.² In fact the spectral output of the dye lasers equipped with the 1200-line/mm gratings was best fit by a Voigt profile composed by convoluting together a Gaussian of width 0.6 cm^{-1} [half width at half maximum (HWHM)] and a Lorentzian of width 0.3 cm^{-1} (HWHM).

This rather complex line-shape function had to be deconvoluted from many of the experimental traces before detailed analysis was possible. Finally, incoherent fluorescence from the dye often contributed a background signal at the output frequency ω_3 . Fortunately, colored glass filters were found to block this fluorescence without noticeably attenuating the laser beam itself.

Standard dyes were employed in ethanol solution for this entire work. Most of this data was obtained using 2-g/liter solutions of rhodamine 6G, rhodamine B, and sodium fluorescein, although coumarin- and oxazole-based dyes were needed for the high-frequency studies of diamond.¹⁷

The output of each laser was split into two beams, and one beam from each laser was focused into each of two material samples. Two optical delay lines insured optimal temporal overlap between the 4-nsec-long dye-laser pulses. Spatial overlap of the 50–100- μm diameter focal spots

was obtained by careful alignment of the mirrors at M and M' .

The incident fields interact constructively over the entire length of the sample whenever the wave-vector mismatch $\Delta K = |2\vec{K}_1 - \vec{K}_2 - \vec{K}_3|$ of the interacting beams is smaller than the inverse of the sample length. This phase-matched condition can readily be obtained by choosing the correct angle between the incident beams. The phase-matching angle depends only weakly upon the frequency difference of the incident fields, and the wave-vector mismatch was readily limited to a values less than the inverse of the sample length as the frequencies were scanned.

One sample, the reference crystal, consisted of a 2-mm- or 5-mm-thick slice of NaCl, a material which lacks both Raman-active optical phonons and low lying electronic excitations. The [001] axis was normal to the surface. The nonlinear susceptibility of NaCl is not expected to vary with $\omega_1 - \omega_2$, and any change in the intensity generated in the signal for NaCl in a three wave mixing results solely from variation in the intensities of the incident beams. Thus each set of pulses was individually calibrated.

The dispersion in the nonlinear susceptibility tensor of the second material was measured as a function of frequency. Generally this unknown sample was expected to have a Raman mode of known frequency and symmetry. By choosing the correct combination of polarization directions for the incident beams and by correctly orienting the sample, one can uniquely measure the intensity generated by various linear combinations of nonlinear susceptibility components.

The liquid samples of reagent-grade benzene were held in 1-cm-length spectroil cells. Care was taken that the incident beams did not overlap at the cell windows. The 5 mm effective sample length was defined by the size of the region in which the incident beams overlapped.⁶

Two type-IIa diamonds were employed in the measurements on that material; one a natural stone previously used in a measurement of electric-field-induced infrared absorption,¹⁸ and the other a synthetic crystal fabricated by General Electric. Both samples were roughly rectangular parallelepipeds of thickness 0.8 mm with large faces perpendicular to the [001] direction. The directions of the cubic axes were determined within 1° by x-ray diffraction. The field at frequency ω_1 propagated along the [001] axis while the field at ω_2 propagated at the phase-matching angle, which was less than 1° away.

The fluoride samples used to measure the dispersion of the nonlinear susceptibilities were 4-mm-thick crystals oriented with a [001] axis normal to the surface. The directions of the other

crystal axes were also determined by x-ray diffraction. The alkaline-earth fluoride samples were cut from synthetic boules supplied by Optovac Corp. The high-resistivity CdF₂ sample were grown in this laboratory and contained 0.003% gadolinium. Again the ω_1 beam propagated along the [001] axis.

The calcite sample upon which measurements of the dispersion of the nonlinear susceptibility were made was a 2-mm-thick plate cut from a natural cleavage. The optic axis was in the plane of the crystal face which was oriented normal to a mirror plane by x-ray diffraction. Another 2-mm-thick crystal with face normal to the optic axis was employed to show the constancy of $\chi_{1221}^{(3)}$. To minimize the effects of birefringence, the propagation directions and field polarizations were carefully defined to be either parallel or perpendicular to the optic axis as required.

Much thinner samples are required to determine the nonlinear susceptibility by the composite sample technique.¹⁹ These thin flakes (~ 0.25 mm thickness) were carefully oriented before grinding to final thickness. In the case of the fluorides, the crystal face was normal to the [111] axis while the calcite flake was oriented with the optic axis parallel to the plane of the plate.

After each sample, both laser beams are blocked by a knife edge. The output beam at ω_3 is collected by a lens and focused into the entrance slit of a 0.25-m tandem monochromator which rejected light elastically scattered by the samples. A 1P28 photomultiplier then converted the light pulse into an electrical pulse for further electronic processing.

Various calibrated neutral density filters placed ahead of the monochromators attenuate the signals in order to prevent saturation of the photomultipliers. When required, a rotatable polarizing filter placed before the entrance slits defined the plane of polarization of the collected signal.

The pulses generated in each channel are averaged by a dual differential boxcar-integrator system. Operational amplifiers then produce a voltage proportional to the logarithm of the ratio of the average pulse heights. In this way fluctuations in the laser output intensities are normalized out of the final data.

To scan over the resonance in the unknown sample, the gratings of the two lasers are rotated by a mechanical linkage in such a way that the frequency difference $\omega_1 - \omega_2$ varies linearly with time while the output frequency $\omega_3 = 2\omega_1 - \omega_2$ remains fixed to avoid potential "roll-off" problems in the monochromators.

The voltage produced by the operational amplifiers is then plotted as a function of time by a chart recorder. The neutral density filters must be occasionally changed to avoid saturation in the photo-

multiplier because of the large dynamic range of the signal from the unknown sample. The resulting trace resembles a log periodic plot of the emitted intensity. The discontinuities resulting from changing the filters can be readily removed by replotting the traces on a simple logarithmic scale.

The noise level on these traces is largely an artifact. It results partly from random variations in the transverse-mode structure of the lasers and partly from periodic fluctuations due to a lack of synchronization between the laser trigger rate and the charging rate of the unregulated nitrogen-laser power supply. Shot noise becomes important only at the lowest signal levels. Long integration times and slow scanning rates reduce the noise level appreciably, but at the price of a significantly slower data-collection rate.

The frequency scales of the three-wave-mixing traces were calibrated against a Jarrel Ash 1-m Ebert monochromator. Each set of data was independently calibrated; the tuning rates varied with wavelength as well as grating order. In all cases, however, the scans were linear within 2%. Backlash in the mechanical linkages and nonlinearities in the grating drive limit the accuracy of the calibration of the difference frequency scale of 4%. The possible systematic errors resulting from the uncertainty in the over-all frequency scale produce the largest contributions to the expected inaccuracies of this experiment. However, since the absolute Raman cross-section measurements published in the literature have estimated uncertainties of 15% and more, the inaccuracies in our frequency measurements are tolerable.

The relative intensity scales were calibrated by obtaining signals in both channels and, with the laser intensities and frequencies fixed, interposing calibrated neutral density filters just before the collection monochromators. The response of the detectors and operational amplifiers was found to be linear within $\pm 5\%$ over a full decade of signal level in each arm of the experiment. This corresponded to two decades in normalized intensity of which only the central decade and a half was ever employed.

Aligning the equipment was a laborious process. First the frequencies of the lasers were set so that $\omega_1 - \omega_2$ corresponded to a strong Raman line in the frequency range of interest. Most useful were the diamond and benzene vibrational modes studied here and the CCl_4 vibration at 460 cm^{-1} . The beams were then overlapped within the resonant sample with crossing angle given by $\Delta K = 0$. The collection lens was adjusted so that the elastically scattered light from the focal region was imaged onto the monochromator slit. The monochromator frequency was then adjusted to maximize the three-wave-mixing signal.

To verify that the pulses observed resulted from three wave mixing, the signal level was observed to drop precipitously to zero at all frequencies when one and then the other of the lasers was blocked. Critical adjustment of the beam crossing angle, collection lens, and sample positions, etc. then results in maximum signal. Correct positioning of the knife edge eliminates the beams at ω_1 and ω_2 . The alignment sample can then be replaced by any desired substance, and a minimal adjustment of the beam crossing angle results again in a near maximum signal. Alignment parameters change only slightly with the frequency difference. Only long samples ($l > 5 \text{ mm}$) occasionally presented difficulty in obtaining perfect phase matching over a large frequency range.

B. Data analysis

The experimental traces as recorded by the chart recorder did not directly yield useful information. The first stage of data analysis was necessarily the elimination of discontinuities resulting from changing the neutral density filters in the collection arms. This was readily accomplished since the changing of such a filter results only in a translation of the signal level along a logarithmic scale. Further, since the filter factors are always known, a simple retracing of the data on an extended intensity scale results in data like that in Fig. 4.

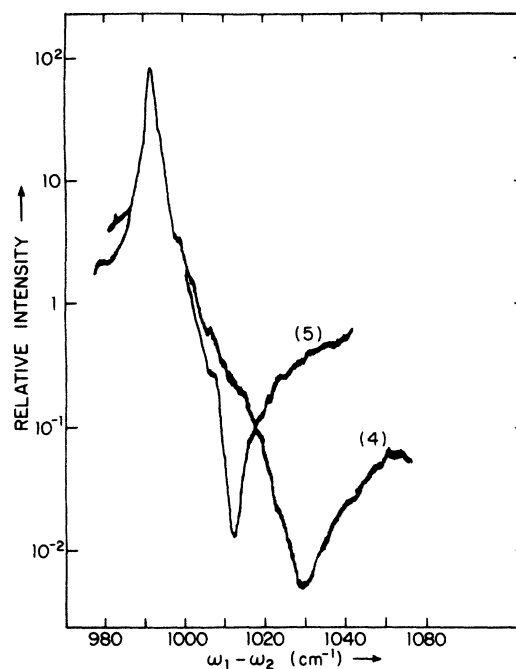


FIG. 4. Typical traces of the intensity emitted at ω_3 by benzene when $\omega_1 - \omega_2 \approx 992 \text{ cm}^{-1}$. The polarizations of the incident beams were at 45° to one another; the numbers denote the corresponding polarization condition in Fig. 2. The traces are normalized to their values far away from resonance. $\lambda_1 = 545 \text{ nm}$.

The horizontal frequency scale was then determined from the frequency calibration runs, and preliminary estimates made of the frequency difference between the maximum and minimum and of the dynamic range spanned by the data.

The experimental data must be compared with the theoretical expression given by Eq. (11). In the case of strong Raman resonances, given very pro-

nounced minima, it was most convenient to assign a prominent role to the frequency separation between maximum and minimum signal. Introducing the shorthand notation

$$\Delta = \frac{N(\alpha^R)^2}{4\hbar \chi_{\text{eff}}} \quad \text{and} \quad \zeta = \Gamma \chi_{\text{eff}}'' / \chi_{\text{eff}}',$$

Eq. (11) can be cast in the form

$$I(\omega_3) = \frac{\{\Delta + \zeta + \omega_0 - (\omega_1 - \omega_2)\}^2 + \{\Gamma - [\omega_0 - (\omega_1 - \omega_2)]\zeta/\Gamma\}^2}{[\omega_0 - (\omega_1 - \omega_2)]^2 + \Gamma^2}. \quad (13)$$

The maximum and minimum in $I(\omega_3)$ occur at the following values for the frequency difference

$$(\omega_1 - \omega_2)_{\text{min,max}} = \omega_0 + \frac{1}{2}(\Delta + \zeta) \pm \frac{1}{2}[(\Delta + \zeta)^2 + 4\Gamma^2]^{1/2}. \quad (14)$$

The frequency difference between maximum and minimum is a measure for the relative strength of the electronic and Raman contributions:

$$\Delta\omega = [(\Delta + \zeta)^2 + 4\Gamma^2]^{1/2}.$$

In the case of diamond, benzene, and calcite the following conditions are satisfied: $\Delta \gg 2\Gamma$ and $\zeta \approx 0$. The maximum occurs at the Raman resonant frequency, and the minimum is upshifted by an amount

$$\Delta\omega = \Delta.$$

It also follows from Eq. (13) that under these conditions the width of the maximum at half-height and the width of minimum at half-depth are both equal to 2Γ .

The width of the minimum is, however, quite sensitive to χ_{eff}'' . The residual intensity at the minimum results entirely from the imaginary part of $\chi^{(3)}$, as the real part of $\chi^{(3)E}$ is cancelled by the negative real part of the Raman susceptibility. If there is no imaginary electronic contribution, the minimum intensity is entirely due to the imaginary part of the Raman term, which is being driven far off resonance. If $\chi_{\text{eff}}''/\chi_{\text{eff}}' > \Gamma/\Delta$ the intensity at minimum—and hence the width at half-depth of the minimum—will be detectably larger than otherwise.

Finally, it should be noted that there are only two free parameters in Eq. (13). The ratio of the real electronic susceptibility to the square of the Raman matrix element and the ratio of the real and imaginary parts of the electronic susceptibility can be adjusted to fit the data. The other parameters,

ω_0 , $|\alpha^R|^2$, and Γ , are extracted from the spontaneous scattering literature. With these data curves of the form Eq. (13) were generated by a Hewlett-Packard 9820 calculator for various values of Δ and ζ . The best possible fit between the maximum and minimum was obtained by varying Δ and the depth of the minimum was fitted by adjusting ζ . Generally, the best fit to any experimental trace (in no case less than three traces for a given polarization and frequency condition were run) agreed within 1 cm^{-1} for the frequency difference between maximum and minimum. The results were averaged. The error in the resonance parameter Δ , for materials with a strong Raman resonance, was estimated from the standard deviation in the data and the fitting accuracy.

For materials with a weak Raman resonance, $\Delta \leq \Gamma$, the frequency difference between maximum and minimum is insensitive to the parameter Δ . In this case, Δ is best determined by fitting the strength of the observed maximum and minimum rather than their frequencies. This latter procedure is more involved since it requires an accurate calibration of the intensity scale and a detailed knowledge of the laser line-shape function. In addition, any drifting of the baseline (which might result from variation of the coherence length or collection efficiency with frequency) leads to uncertainties in the result.

The first step in the analysis of the three-wave-mixing traces of CaF_2 and its analogs was an estimate of the enhancement of the signal at maximum, and its depression at minimum. The frequency difference between maximum and minimum was also measured and any difference between the observed value and 2Γ noted.

The observed intensity as a function of the difference of the incident frequencies was then fit to a function of the form

$$I(\omega_1 - \omega_2) = \left| \int g(\omega_1 - \omega_2 - \omega') \left(1 - i\zeta\Gamma^{-1} + \frac{\Delta}{\omega_0 - \omega' + i\Gamma} \right) d\omega' \right|^2, \quad (15)$$

where ζ and Δ are the two free parameters. All else is determined from spontaneous Raman scattering or spectroscopic resolution of the incident laser line shapes.

The line-shape function $g(\omega)$ above is formally the spectral density function of the nonlinear force term $\alpha_{ij,\sigma}^R E_i(\omega_1) E_j(-\omega_2)$.¹¹ If the output of the two incident lasers are totally uncorrelated, $g(\omega)$ is given by

$$\begin{aligned} g(\omega) &= \int dt e^{-i\omega t} \langle E_1(t) | E_1^*(0) \rangle \langle E_2(t) | E_2^*(0) \rangle \\ &= \int d\omega' f_1(\omega - \omega') f_2(\omega'), \end{aligned} \quad (16)$$

where $E_1(t)$ and $E_2(t)$ are the electric fields emanating from laser 1 and 2, respectively, and $f_1(\omega)$ and $f_2(\omega)$ are the spectral density (line-shape) functions of the individual lasers.

These line-shape functions were determined by resolving the laser output using the same 1-m Ebert monochromator employed to calibrate the frequency scales. The line-shape function of the monochromator itself was determined by scanning the profiles of the 5460- and 5770-Å lines of a low-pressure mercury lamp. The nearly negligible distortions of the laser line shape produced by the finite resolution of the instrument were easily deconvoluted.

The laser line-shape function thus determined was found to approximate a Voigt profile quite accurately:

$$\begin{aligned} f(\omega) &= \frac{(\ln 2)^{1/2}}{\pi^{3/2} \epsilon} \int d\omega' \\ &\times \exp \left[-\ln 2 \left(\frac{\omega - \omega'}{\epsilon} \right)^2 \right] \frac{\gamma}{\omega'^2 + \gamma^2} \end{aligned} \quad (17)$$

with parameters $\gamma = 0.4 \pm 0.15 \text{ cm}^{-1}$, $\epsilon = 0.6 \pm 0.1 \text{ cm}^{-1}$, when 1200-lines/mm gratings were employed, and $\gamma = 0.35 \pm 0.25 \text{ cm}^{-1}$, $\epsilon = 0.35 \pm 0.1 \text{ cm}^{-1}$ with 600 lines/mm gratings. This implies that the nonlinear line-shape function $g(\omega)$ is also well approximated by a Voigt profile, but with parameters $\gamma = 0.8 \pm 0.4 \text{ cm}^{-1}$, $\epsilon = 0.9 \pm 0.1 \text{ cm}^{-1}$ for the 1200 lines/mm gratings. With the better gratings, the laser linewidth could be ignored.

The function in Eq. (17) could then be numerically evaluated using the same programmable plotting calculator employed to generate previous theoretical curves. The two free parameters, Δ and ζ , were optimized for each of the experimental traces. The best values (found by visually comparing theoretical and experimental curves) were averaged. Errors were estimated by determining the "worst acceptable fit" and adding the deviation of the parameters describing that curve from those describing the "best fit" to the standard deviation of the best-fit data.

The treatment so far is strictly applicable to homogeneously broadened Raman resonances. Inhomogeneous broadening, e.g., due to crystal strains, could be taken into account by an integration of each result over a distribution of resonant frequencies ω_0 . This was considered unnecessary as phenomenological values for the width Γ were used, which may include an inhomogeneous contribution.

In the case of diamond and benzene the value of Δ was determined for all five geometries in Fig. 2, corresponding to five different values for the effective electronic susceptibility χ_{eff} . Table I shows that only three independent quantities d_1 , d_2 , and d_3 are involved in diamond, corresponding to the three independent tensor elements for $\chi^{(3)E}$. For benzene, also, three independent quantities are involved, if in addition to the two independent elements of $\chi^{(3)E}$, the depolarization ratio ρ is considered an unknown quantity. The problem is overdetermined and a multiple linear regression program was used to obtain the best possible fit. The experimental curves for diamond with the five polarization geometries are shown in Fig. 5 with the fitted curves. The experimental and fitted values

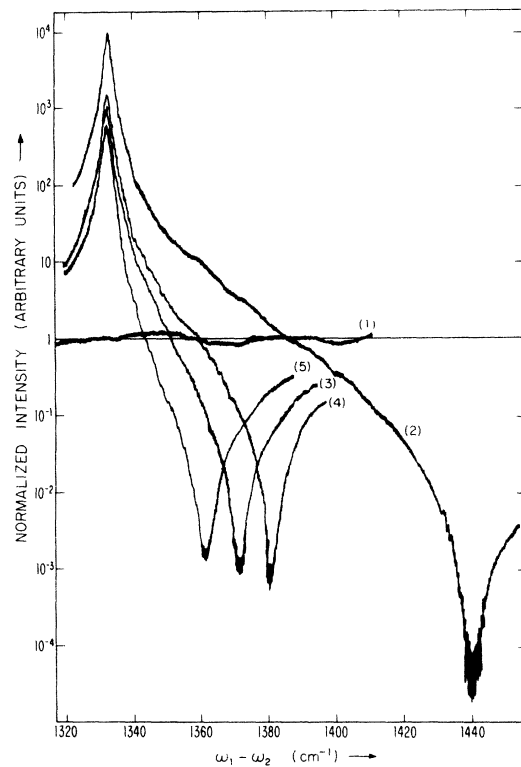


FIG. 5. Three-wave-mixing traces for diamond for $\omega_1 - \omega_2$ near the 1332- cm^{-1} Raman line. The numbers in parentheses refer to the polarization conditions in Fig. 2. The intensities are normalized to unity far from the Raman resonance. $\lambda_1 = 545 \text{ nm}$.

TABLE II. Experimental and fitted resonance strengths Δ for benzene and diamond at $\lambda_1 = 545$ nm.

Polarization condition	Benzene		Diamond	
	Δ_{exp}^a (cm ⁻¹)	Δ_{fit} (cm ⁻¹)	Δ_{exp}^a (cm ⁻¹)	Δ_{fit} (cm ⁻¹)
1	25.6 ± 0.5	26.0	N. R. ^b	N. R.
2	1.3 ± 0.5	1.5 ± 0.4	109 ± 1	109
3	25.6 ± 0.5	26.0	39.5 ± 1	37.4
4	37.3 ± 0.5	36.8	49.0 ± 1	50.7
5	20.3 ± 0.5	20.1	29.0 ± 1	29.6

^aSystematic errors not included.

^bN. R. means no resonance.

of Δ are shown in Table II for both benzene and diamond.

The value of the Raman parameter $N(\alpha^R)^2$ was taken from spontaneous cross-section experiments reported in the literature. In the case of total symmetric vibration of benzene, the classic work of Skinner and Nilson provided an accurate absolute calibration.²⁰

The data for diamond was most plentiful, but also somewhat contradictory. Furthermore, the experiments quoted in the literature were performed at incident frequencies considerably below those used in much of this work.^{16,21,22} One might well expect that the Raman matrix element itself should vary with frequency over the range studied here in diamond. We therefore fit all the available matrix-element data for diamond to a functional form

$$|\alpha_{12,s}^R| = \frac{x^2}{E_- - \hbar\omega_1}, \quad (18)$$

with E_- the energy of the direct energy gap in diamond at 9 eV. Equation (3) then predicts a value for the Raman matrix element of $|\alpha^R|^2/4\hbar c = (5.6 \pm 0.6) \times 10^{-12}$ esu cm⁻¹ for $\lambda_1 = 545$ nm. This is rather above the value quoted previously, but in better agreement with the bulk of the experimental data.⁵ If, however, one chooses the center of gravity of the absorption bands as determined by Sellmeyer's formula as the energy E_- in Eq. (18) (~ 12 eV), all values for $|\alpha^R|^2$ must be reduced by one error bracket.

Data for the Raman cross section in calcite have been measured both absolutely and relatively to the benzene, with reasonable consistency.^{22,23} No cross-section measurements were available for the weak Raman modes of the CaF₂-structure materials. In this case the electronic nonlinearity was measured relative to the calcite Raman mode by the composite-sample technique, and the Raman contribution normalized to the electronic term.¹⁹ The three-wave-mixing traces were then employed to calculate the relative values of the different components of the electronic nonlinearity. Because of the reduced accuracy necessitated by the

weak Raman modes in these ionic crystals, Kleinman's condition was assumed to be satisfied within the experimental accuracy.

With the fitted values of Δ and the known Raman cross section, the tensor components of the electronic nonlinear susceptibility are determined. The greatest uncertainty results from the Raman cross section. Therefore, relative values of $\chi^{(3)}$ components are more accurate. In our tables of results the estimated error values in parentheses include the uncertainty in the Raman cross sections while those quoted without parentheses do not. In Sec. IV the results will be presented and discussed.

IV. EXPERIMENTAL RESULTS AND DISCUSSION

A. Benzene

The dispersion of $\chi_{1111}^{(3)}$ and $\chi_{1221}^{(3)}$ in benzene was reported previously,⁶ but for a complete parametrization of all components of the electronic nonlinearity one must employ the orientation conditions with the incident fields at 45° rather than 0° or 90°. The experimental curves are shown in Fig. 4 for the geometries 4 and 5 of Fig. 2.

Table II lists the values of Δ determined for each of the orientations in benzene. Fitting these numbers with Eq. (12) and the appropriate d constants resulted in values for the electronic nonlinearity components tabulated in Table III.

Kleinman symmetry would predict that $\chi_{1122}^{(3)E} = \chi_{1221}^{(3)E}$. Experimentally we find that $\chi_{1122}^{(3)E}/\chi_{1221}^{(3)E} = 1.2 \pm 0.1$. $\chi_{1111}^{(3)} - \chi_{1221}^{(3)} - 2\chi_{1122}^{(3)}$ is, of course, rigorously zero in the isotropic liquid. The violation of Kleinman's condition results partly from the contributions to $\chi^{(3)}$ from other vibrational modes and partly from the fact that with the frequencies employed, $2\omega_1$ is *not* far below the electronic transition frequencies. Nevertheless, it appears that Kleinman symmetry is accurate to about 20% in this frequency range.

It is clear from Figs. 2 and 4 that the polarization direction of the wave emitted at ω_3 varies with frequency when the incident fields are at 45° to one another. In general, the emitted wave will be elliptically polarized, but at most frequencies it is nearly plane polarized and the plane of the major axis can always be defined. We measure the angle made by this plane with the polarization direction of the incident fields as a function of frequencies. A Glan prism ahead of the sample monochromator was rotated until the emitted wave was extinguished. Figure 6 shows the results. Far from the resonance, the angle extrapolates towards $\tan^{-1}\frac{1}{2}$ as predicted by Kleinman symmetry. As $\omega_1 - \omega_2$ moves through the resonance the polarization direction changes dramatically, covering a full 180° in the range of 100 cm⁻¹. This is because the Raman susceptibility has a different ratio between the tensor components than $\chi^{(3)E}$. At resonance

TABLE III. Nonlinear parameters of cubic crystals and benzene.

Material	wavelength λ_1 (nm)	$\frac{N \alpha^R ^2}{4hc}$ (10^{-13} cm $^{-1}$ esu)	$\chi_{1111}^{(3)E}$ (10^{-14} esu)	$\chi_{1221}^{(3)E}$ (10^{-14} esu)	$\chi_{1122}^{(3)E}$ (10^{-14} esu)	$\chi_{1111}^{(3)E}$ (10^{-14} esu)	$\chi_{1221}^{(3)E}$ (10^{-14} esu)
Benzene	545	14.4 (± 1)	1.84 \pm 0.08 (± 0.15)	0.54 \pm 0.03 (± 0.05)	0.65 \pm 0.04 (± 0.07)	< 0.02	< 0.002
Diamond	545	56.2 (± 6)	4.60 \pm 0.2 (± 0.6)	1.72 \pm 0.06 (± 0.18)	1.84 \pm 0.08 (± 0.2)	< 0.04	< 0.005
CaF ₂	575	0.53 (± 0.11)	0.43 \pm 0.13 (± 0.16)	0.19 \pm 0.05 (± 0.06)		< 0.02	< 0.01
SrF ₂	575	0.84 (± 0.27)	0.44 \pm 0.10 (± 0.13)	0.30 \pm 0.04 (± 0.06)		0.07 \pm 0.02	0.04 \pm 0.01
CdF ₂	575	1.07 (± 0.25)	1.45 \pm 0.22 (± 0.32)	0.47 \pm 0.07 (± 0.10)		< 0.2	< 0.02
BaF ₂	575	1.87 (± 0.36)	0.83 (± 0.09) (± 0.16)	0.34 \pm 0.03 (± 0.06)		0.3 \pm 0.1	0.06 \pm 0.02

$P(\omega_3)$ is parallel to $E(\omega_1)$ as would be expected for the dominant contribution from a totally symmetric Raman mode. The large error brackets are in the region of minimum eccentricity of the polarization ellipse, and reflect the experimental difficulties of defining the plane of the major axis under these conditions. The effect shown in Fig. 6 may be designated as a dispersion of the plane of polarization. It illustrates how sensitive the ratio of the various tensor elements of $\chi^{(3)}$ are in the vicinity of a resonance at a combination frequency. Off resonance the polarization is strictly linear and the angle ϕ is given by

$$\tan\phi = \frac{P_x(\omega_3)}{P_y(\omega_3)} = \frac{2\chi_{1122}^{(3)}}{\chi_{1111}^{(3)} + \chi_{1221}^{(3)}}. \quad (19)$$

Using the isotropy condition and the Kleinman symmetry this angle becomes

$$\phi = \arctan \frac{1}{2}$$

in agreement with the experimental data.

At the Raman resonance the nonresonant term may be ignored. The Raman susceptibilities are all pure imaginary. Since $\chi_{1221}^{(3)E} = 0$, and the isotropy condition must still be satisfied, so that

$$\chi_{1111}^{(3)R} = 2\chi_{1122}^{(3)R} \text{ one obtains}$$

$$\phi = \arctan 1 = 45^\circ.$$

At the Raman resonance the polarization of the output at ω_3 is parallel to the field at $E(\omega_1)$, in agreement with the observation.

B. Diamond

The previous study of the dispersion of the nonlinear susceptibility of diamond has been extended to determine the values of all the independent components of the electronic nonlinearity and plot their

variation with frequency.⁵ To this end, the variation of the emitted intensity was measured in all five polarization conditions of Fig. 2. The agreement between the theory and all experimental curves is less close than the case of benzene because of the difficulty of orienting a crystalline substance with respect to the electric field directions within the necessary $\pm 0.5^\circ$. Values of the electronic nonlinear susceptibility components deduced in this manner along with the value of the Raman matrix element employed appear in Table III.

Kleinman symmetry is obeyed rather better in diamond than in benzene. Our result is

$$\chi_{1221}^{(3)E} / \chi_{1122}^{(3)E} = 1.07 \pm 0.06.$$

The anisotropy parameter for the cubic polarizability is

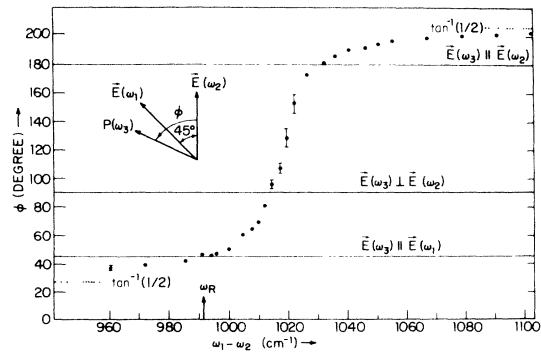


FIG. 6. Rotation of the plane of polarization of the beam at ω_3 generated by benzene as $\omega_1 - \omega_2$ passes through the frequency of the 992-cm $^{-1}$ Raman mode (arrow). The inset shows the definition of polarization angle and the polarization of the incident beams. $\lambda_1 = 545$ nm.

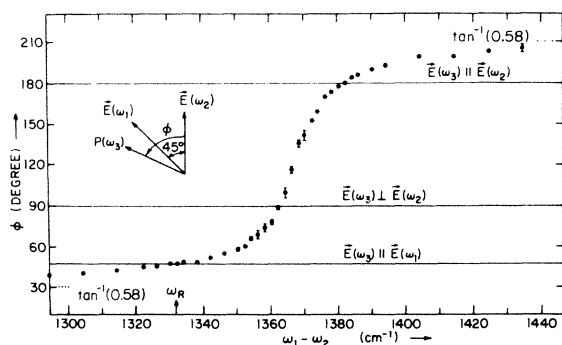


FIG. 7. Rotation of the plane of polarization of the radiation emitted by diamond at ω_3 as $\omega_1 - \omega_2$ passes through the Raman resonance at 1332 cm^{-1} (arrow). The inset shows the definition of the polarization angle and the polarization direction of the incident beams. $\lambda_1 = 545 \text{ nm}$.

$$\sigma = \frac{2\chi_{1122}^{(3)E} + \chi_{1221}^{(3)E} - \chi_{1111}^{(3)E}}{\chi_{1111}^{(3)E}} = 0.17 \pm 0.05, \quad (20)$$

rather less than in other tetrahedrally bonded crystals.⁸ This does not imply that the material is isotropic, but rather that the electrons responsible for $\chi^{(3)}$ inhabit nearly spherical orbitals.⁷ When the incident fields are polarized at 45° to one another, the polarization direction at ω_3 is again a sensitive function of the frequency difference. Figure 7 shows the dispersion of the polarization direction. At the Raman resonance the polarization $P(\omega_3)$ is again parallel to $E(\omega_1)$, because in this case

$$\chi_{1111}^{(3)R} = 0 \quad \text{and} \quad \chi_{1221}^{(3)R} = 2\chi_{1122}^{(3)R}.$$

Far off resonance the above quoted anisotropy leads to

$$\phi = \arctan 0.58 = 30^\circ$$

in reasonable agreement with the observed value.

In order to show the dispersive behavior of $\chi^{(3)E}$ three-wave-mixing traces of diamond were taken in polarization conditions 2 and 3 for five pairs of incident wavelengths. The incident frequencies were chosen so that $\omega_1 - \omega_2$ corresponds to the region of the phonon frequency while ω_1 varied from $\hbar\omega_1 < \frac{1}{2}E_g$ to $\hbar\omega_1 > \frac{1}{2}E_g$, where E_g is the energy of the indirect band gap of diamond at 5.4 eV .²⁴

The values of Δ are plotted in Fig. 8 as a function of twice incident photon energy $2\hbar\omega_1$. Since Δ is proportional to the ratio of the square of the Raman matrix element to the electronic nonlinearity, the systematic decrease of Δ indicates that the electronic nonlinearity increases more rapidly with frequency than the Raman matrix element. If the matrix element and electronic nonlinearity scale with frequency as predicted in Eqs. (2) and (18), Δ then scales as $E_+ - 2\hbar\omega_1$, where E_+ is the aver-

age difference in energy between electronic bands of the same parity. The solid lines in Fig. 8 are least square fits of that form to the data. They indicate values of $E_+ = 12.5 \pm 1 \text{ eV}$.

Figure 9 shows a three-wave-mixing trace of diamond for $2\hbar\omega_1 = 6.08 \text{ eV}$, well above the indirect band gap. The distinct filling in of the minimum results from two-photon absorption. The linear absorption parameter at this energy is $\sim 6000 \text{ cm}^{-1}$, but the value for ζ which best fits this data is $0.05 \pm 0.02 \text{ cm}^{-1}$.²⁴ This implies $\chi_{1221}^{(3)E''} = (0.18 \pm 0.05) \times 10^{-14} \text{ esu} < \chi_{1221}^{(3)E'}$. Similarly we also find

$$\frac{1}{2}(\chi_{1111}^{(3)E''} + \chi_{1221}^{(3)E''} + 2\chi_{1122}^{(3)E''}) = (0.40 \pm 0.15) \times 10^{-14} \text{ esu}.$$

Values for Δ observed for various input energies along with assumed values of the Raman matrix elements and deduced electronic nonlinearity parameters for diamond appear in Table IV. The values quoted in this table are in the convention of Maker and Terhune. Previous work quoted in Refs. 5 and 10 used a different definition of $\chi^{(3)}$ which resulted in numbers four times larger. The large changes in $\chi^{(3)E}$ occurring in a transparent region of a material implies a large contribution from near resonant virtual transitions like those in Fig. 1(b). One must employ care when applying nonlinear susceptibility data measured at one frequency in the analysis of an experiment at another. In particular, the estimates of the nonlinear sus-

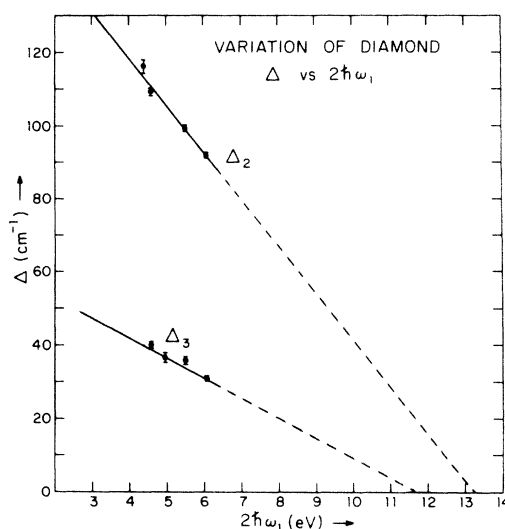


FIG. 8. Variation of the frequency difference between minimum and maximum intensity observed in three wave mixing in diamond as a function of $2\hbar\omega_1$. The subscripts on Δ refer to the polarization condition in Fig. 2. The extrapolations of the lines that best fit these data points cross zero at approximately $12\text{--}13 \text{ eV}$. That energy may represent an average band gap for electronic states of the same parity.

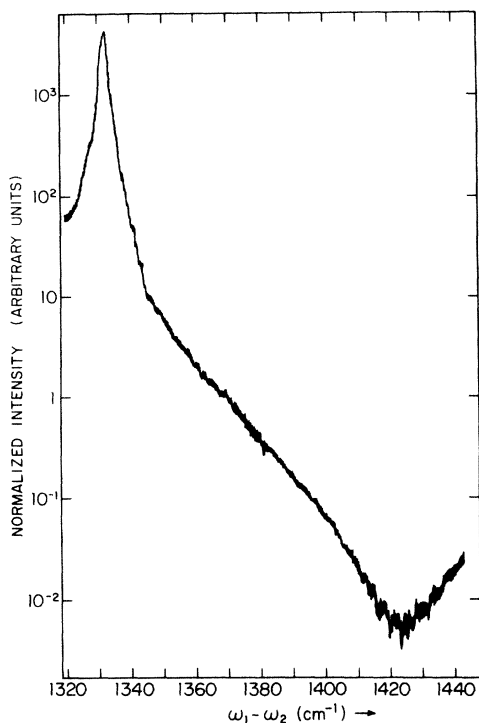


FIG. 9. Typical three-wave-mixing trace for diamond in polarization condition 2 and $\lambda_1 = 407$ nm. The noticeable filling-in and broadening of the minimum compared to Fig. 5 indicates an imaginary contribution to $\chi_{1221}^{(3)E}$ due to two-photon-absorbing processes.

ceptibility of diamond for $2\hbar\omega_1 \approx 3.2$ eV quoted in Ref. 10 are significantly smaller than the values in Table IV. The discrepancy results from the frequency dispersion shown in Fig. 8 as well as from a reduced value of the Raman matrix element.

The second order spontaneous Raman spectrum of diamond contains a strong sharp feature at 2666 cm^{-1} , slightly above the frequency of two $k=0$

optical phonons.²⁵ In an attempt to observe the dispersion of $\chi^{(3)}$ related to this feature, lasers beams of frequency

$$21\,053\text{ cm}^{-1} < \omega_1 < 21\,119\text{ cm}^{-1},$$

$$18\,302\text{ cm}^{-1} < \omega_2 < 18\,508\text{ cm}^{-1},$$

were mixed in polarization condition 3. In spite of the large crossing angle required for phase matching, adequate signal was obtained at $\omega_1 = 23\,800$ cm^{-1} .

No dispersion of $\chi^{(3)}$ attributable to the second-order Raman effect was observed. Variations in the coherence length and optimal crossing angle with difference frequency $\omega_1 - \omega_2$ contributed a considerable drift of the baseline with frequency, but the value of $\chi^{(3)}$ was observed to be constant to $\pm 25\%$ over the frequency range expected to include the second-order Raman structure.

Spontaneous cross-section measurements indicate that the second-order feature in diamond has roughly 300 times less integrated intensity than the first-order Raman line. Estimates of the expected variation in the intensity observed at ω_3 based upon Eq. (13) and the data in Table VI indicate that a 30% variation should have been expected at most. The actual dispersion caused by a second-order Raman feature depends upon the symmetry character of the phonon modes involved; these negative findings are consistent with the spontaneous cross section and symmetry information.

C. Calcium fluoride and analogs

In an attempt to measure the variation of the nonlinear susceptibility with atomic number in a series of homologous crystals, three-wave-mixing experiments were performed upon CaF_2 , SrF_2 , CdF_2 , and BaF_2 . The electronic nonlinearity was first measured relative to the Raman susceptibility of the calcite 1088-cm^{-1} mode via the composite-

TABLE IV. Nonlinear parameters of diamond for various frequencies, $\omega_R = 1332$ cm^{-1} , $\Gamma = 1.04$ cm^{-1} .

Wavelength λ_1 (nm)	$\frac{N \alpha^R ^2}{4hc}$ (10^{-13} esu cm^{-1})	Δ_2 (cm^{-1})	Δ_3 (cm^{-1})	$\chi_{1221}^{(3)E}$ 10^{-14} esu	$\frac{1}{2}(\chi_{1111}^{(3)E} + 2\chi_{1122}^{(3)E} + \chi_{1221}^{(3)E})$ (10^{-14} esu)
565	54.9 (± 6)	116 ± 4	43.3 ± 1.4	1.58 ± 0.06 (± 0.18)	4.23 ± 0.2 (± 0.45)
545	56.2 (± 6)	109 ± 4	39.5 ± 1.5	1.72 ± 0.04 (± 0.18)	4.71 ± 0.16 (± 0.51)
500	59.9 (± 6)		36.1 ± 1.5		5.5 ± 0.2 (± 0.65)
450	65.2 (± 7)	99.3 ± 4	35.4 ± 1	2.19 ± 0.04 (± 0.25)	6.1 ± 0.2 (± 0.65)
407	71.9 (± 8)	92 ± 4	30.3 ± 1	2.61 ± 0.06 (± 0.30)	7.91 ± 0.2 (± 0.84)

TABLE V. Nonlinear parameters of CaF₂ structure crystals at $\lambda_1 = 575$ nm.

Material	T (°K)	ω_R (cm ⁻¹)	Γ (cm ⁻¹)	$\frac{1}{2}(\chi_{1111}^{(3)} + 2\chi_{1122}^{(3)} + \chi_{1221}^{(3)})$ (10 ⁻¹⁴ esu)	$\frac{N \alpha^R ^2}{4hc}$ 10 ⁻¹⁴ cm ⁻¹ esu	Δ_2 (cm ⁻¹)	Δ_3 (cm ⁻¹)	σ^a
CaF ₂	295	322	3.5	0.49 ± 0.05 (± 0.09)	4.0 ± 1.0 (± 1.5)	9.3 ± 0.9	2.7 ± 0.5	-0.1 ± 0.4
	77	326	0.75		5.3 ± 0.7 (± 1.7)	9.5 ± 0.3	3.6 ± 0.3	0.3 ± 0.4
SrF ₂	295	285	3.5	0.66 ± 0.05 (± 0.12)	7.0 ± 0.9 (± 2.1)	10.2 ± 1.0	3.5 ± 0.4	0.1 ± 0.3
	77	288	0.75		10.0 ± 0.9 (± 2.1)	11.2 ± 0.3	5.0 ± 0.3	1.0 ± 0.5
CdF ₂	295	322	7.0 ± 1.5	1.43 ± 0.15 (± 0.27)	10.8 ± 1.9 (± 2.5)	6.5 ± 1.0	2.2 ± 0.5	0.0 ± 0.3
	77	324	2.0 ± 0.5			7.7 ± 0.6	2.5 ± 0.2	0.0 ± 0.3
BaF ₂	295	240	3.5	0.92 ± 0.07 (± 0.16)	18.7 ± 2 (± 3.6)	17.7 ± 0.7	6.8 ± 0.7	0.4 ± 0.3
	77	242	0.75			18.5 ± 0.5	6.8 ± 0.5	0.23 ± 0.15

^aSee Eq. (20).

crystal technique.¹⁹

The composites consisted of a 0.25-mm-thick calcite plate and a 0.25-mm-thick fluoride sample. The [110] axis of the fluoride was perpendicular to the optic axis of the calcite. The incident and generated fields were also perpendicular to the optic axis of the calcite. By measuring the shift of the frequency of minimum intensity between the composite sample and calcite, the nonlinear susceptibility $\frac{1}{2}(\chi_{1111}^{(3)} + 2\chi_{1122}^{(3)} + \chi_{1221}^{(3)})$ of the fluorides could be determined. Since this Raman mode of calcite lies well above the phonon frequencies of the fluorides, the nonlinearity thus determined is the electronic contribution.

The results appearing in Table V show that there is, as expected a systematic increase in the electronic nonlinearity with atomic number. The value obtained for CdF₂ is less consistent with this trend, but the difference observed is attributable to the contributions of *d* electrons absent in the alkaline-earth elements.

All of these fluorides show Raman modes of relatively low frequency ($240 \text{ cm}^{-1} < \omega_2 < 326 \text{ cm}^{-1}$) and large linewidth ($\Gamma = 3.5 \text{ cm}^{-1}$ at room temperature).²⁶ The dispersion of the nonlinear susceptibility due to these phonons were measured in all of the materials in polarization conditions 2 and 3. Typical data appear in Fig. 10. From the values of the resonance parameter Δ found in the two orientations, we were able to calculate the electronic anisotropy σ . Further, using the data on the electronic nonlinearities determined by the composite-crystal techniques and Eqs. (12) and (13) we estimated the values of the diagonal and off-diagonal

electronic nonlinear susceptibilities $\chi_{1111}^{(3)E}$ and $\chi_{1221}^{(3)E}$ as well as the Raman matrix element, $\alpha_{12,3}^R$. The results are tabulated in Table V.

Spontaneous scattering measurements indicated that the linewidths of the fluoride Raman modes could be substantially reduced by lowering the crystal temperatures to 77 °K.²⁶ A three-wave-mixing trace taken at cryogenic temperatures is shown in Fig. 11. It displays more pronounced resonant features as was expected. Since $\Delta \geq 2\Gamma$

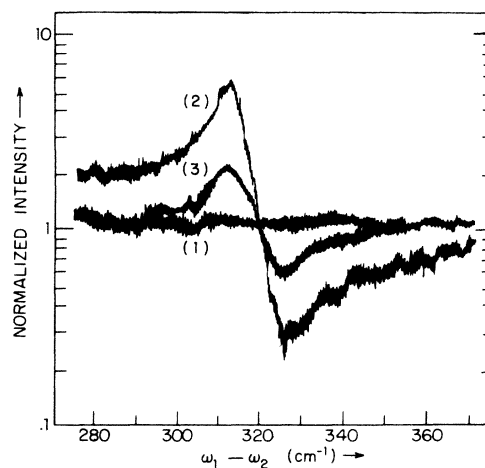


FIG. 10. Three-wave-mixing traces for CaF₂ at 300 °K. The numbers in parentheses again refer to polarization conditions. The relatively weak dispersion due to the Raman modes of these highly ionic crystals necessitates more refined data-reduction procedures. $\lambda_1 = 575$ nm.

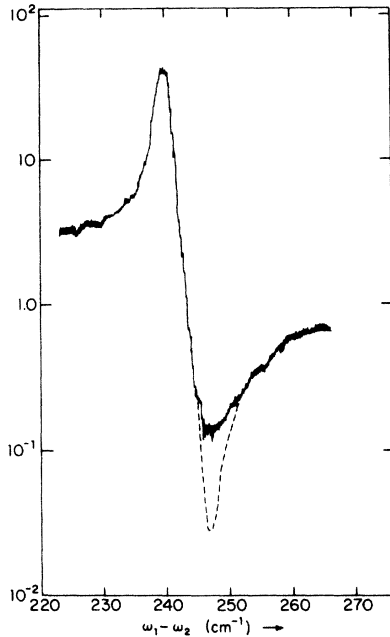


FIG. 11. A typical trace for BaF_2 in polarization condition 3 at 77 °K. Low temperatures reduce the linewidth of the Raman mode and enhance the dispersion. The broadening of the minimum indicates an imaginary contribution to $\chi^{(3)E}$ from two-photon-absorbing processes. The dashed line shows the expected line shape were this contribution absent. $\lambda_1 = 572$ nm.

at 77 °K, an improved value of the resonance strength Δ could be obtained from the frequency difference between maximum and minimum. Only minor changes in the ratio of the Raman matrix elements to the electronic nonlinearities were found. The differences between values of Δ_i for the same material at different temperatures and tabulated in Table V reflect mostly experimental uncertainties.

An unexpected result of this investigation was the excessive intensity which appeared at the frequency of the minimum in the SrF_2 and BaF_2 traces. In a transparent material with a single Raman mode, the imaginary nonlinear susceptibility needed to account for this intensity can only result from two-photon absorption. While these crystals are not entirely transparent at $2\hbar\omega_1$, the linear absorption is much less than it is in diamond at energies at which diamond shows similar two-photon-absorption cross sections.

The imaginary part of $\chi^{(3)E}$ which appears in Table III was obtained by fitting the resonance curves with the function in Eq. (18). No measurable variation in the imaginary part was found as a function of temperature.

In an attempt to find whether the nonzero $\chi^{(3)E''}$ observed in SrF_2 and BaF_2 was an intrinsic or impurity effect, three-wave-mixing traces were tak-

en of CaF_2 doped with 1.2-at. % Gd^{3+} . This crystal showed sharp linear absorption lines at 273.6, 273.9, 275.8, and 278.8 nm with linear absorption constants of ~ 1 cm^{-1} . Three-wave-mixing traces taken in polarization conditions 3 at 77 °K with $\lambda_1 = 551.6$ nm (corresponding to two-phonon absorption by the 275.8 nm line) showed no filling-in of the minimum in the Raman line shape due to $\chi^{(3)E''}$. Dispersive behavior was not observed due to these potential two-photon-absorption transitions.

The absence of a detectable contribution to $\chi^{(3)}$ due to these gadolinium impurity lines indicates that the values of $\chi^{(3)E''}$ observed in SrF_2 and BaF_2 are intrinsic to these crystals. Impurity concentrations much above 1% seem unlikely in these supposedly pure samples. Selection rules should permit observation of some linear absorption from any impurity contributing strongly to nonlinear absorption. No substantial impurity lines appear in the linear absorption spectrum. The relatively large values of $\chi^{(3)E''}$ observed at low frequencies in SrF_2 and BaF_2 imply the existence of low lying excited electronic states with the same parity as the valence band in these crystals. This situation is in sharp contrast to that in diamond where all of the low lying excited states have opposite parity to the valence band.

D. Calcite

The dispersion of $\chi_{1111}^{(3)}$ in calcite has been reported previously¹⁹; Fig. 12 shows the dispersion of $\chi_{3333}^{(3)}$ and $\chi_{1221}^{(3)}$ along with theoretical curve of the form in Eq. (13). As expected, no resonance appeared in $\chi_{1221}^{(3)}$ which was probed by propagating ω_1 down the optic axis with $E(\omega_1)$ and $E(\omega_2)$ in principal planes. The birefringence of calcite caused some difficulty in phase matching the three-wave-mixing process in the $\chi_{1133}^{(3)}$ orientation condition. The emitted intensity was quite weak. Nevertheless, from the asymmetry of the observed spectrum, we have determined that the electronic susceptibility component $\chi_{1133}^{(3)}$ has the same sign as the product of Raman matrix elements $\alpha_{11,A}^R \alpha_{33,A}^R$. If the bonding orbitals in the CO_2 ion filled the same volume while the oxygen nuclei oscillated, the signs would have been opposite.

Table VI gives the values of Δ observed in three wave mixing in calcite. The electronic nonlinear susceptibilities may be estimated from this data and the matrix element $\alpha_{11,A}^R$ by observing that $(\alpha_{33,A}^R)^2 = 0.2 (\alpha_{11,A}^R)^2$.²⁷ Again the error estimates in parentheses reflect the full uncertainties of the calculation while the errors quoted without parentheses are those of this experiment.

E. Trends of $\chi^{(3)E}$

The diverse and accurate data obtained in this investigation should stimulate attempts to relate the

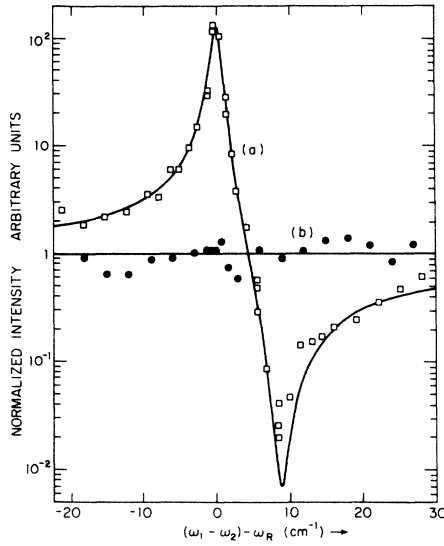


FIG. 12. Variation of the three-wave-mixing intensity in calcite. Dispersion of $|\chi_{3333}^{(3)}|^2$ is shown as trace (a), that of $|\chi_{1221}^{(3)}|^2$ as trace (b) for $\omega_1 - \omega_2$ near the 1088- cm^{-1} Raman mode. As expected, no variation in $|\chi_{1221}^{(3)}|$ results from the totally symmetric vibration of the CO_3 ion (black dots), whereas the dispersion of $|\chi_{3333}^{(3)}|$ (open squares) closely parallels the predicted line shape. The emitted intensity is normalized to its value far from resonance. $\lambda_1 = 530 \text{ nm}$.

values of the nonlinear susceptibilities to other material parameters. As expected, materials with larger linear susceptibilities have larger nonlinear susceptibilities. Materials in which the electrons inhabit extended orbitals have a larger hyperpolarizability (nonlinear susceptibility per formula unit uncorrected for local-field effects) than those consisting of more tightly bound ionic cores. The electronic nonlinearity increases as $2\hbar\omega_1$ approaches the band gap for two-photon-absorption processes. This last effect can be quite pronounced, and is not taken into account in many simple models. The anharmonic oscillator model of Glass *et al.*¹⁴ attempts to correlate $\chi^{(3)}$ with the linear index of refraction and an effective resonant frequency ω_0 according to the Sellmeyer equation. In Fig. 13 we have plotted $\frac{1}{2}(\chi_{1111}^{(3)E} + 2\chi_{1122}^{(3)E} + \chi_{1221}^{(3)E})$ for the cubic and isotropic materials investigated

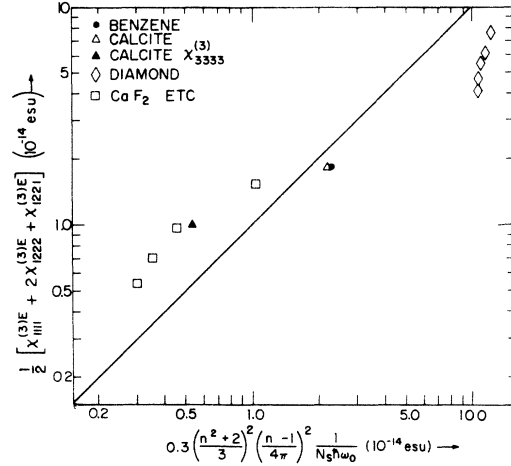


FIG. 13. A correlation plot of the observed values of

$$\frac{1}{2}(\chi_{1111}^{(3)E} + 2\chi_{1122}^{(3)E} + \chi_{1221}^{(3)E}) \text{ vs } 0.3 \left(\frac{n^2 + 2}{3}\right)^2 \left(\frac{n-1}{4\pi}\right)^2 (2\hbar\omega_0)^{-1}.$$

The phenomenological rule proposed in Ref. 14 would predict a proportionality between these quantities for all materials. The squares correspond to the CaF_2 -structure crystals, the diamonds to diamond at a variety of wavelengths, and the circle and triangles to benzene and calcite, respectively.

in this paper against the quantity suggested by that model. We have also added the data points for $\chi_{3333}^{(3)E}$ and $\chi_{1111}^{(3)E}$ in calcite. If the model were strictly applicable, the points should fall on the straight line. The data for diamond represent different frequencies ω_1 . It is obvious that the model even with an adjustable anharmonicity has only qualitative significance, and can certainly not be relied upon to predict the dispersive features of $\chi^{(3)E}$.

V. CONCLUSION

With tunable pulsed dye lasers of high peak power it is possible to investigate details of the dispersive behavior of $\chi^{(3)}$, so that one may speak of nonlinear spectroscopy of crystals and liquids. A systematic extension of the pioneering work of Maker and Terhune appears worthwhile.

The interference effects which occur when $\omega_1 - \omega_2$ is close to the frequency of a strong and sharp Raman vibrations may be used to measure

TABLE VI. Nonlinear parameters of calcite, $\omega_R = 1088 \text{ cm}^{-1}$, $\Gamma = 0.75 \text{ cm}^{-1}$.

Orientation	Wavelength λ_1 (nm) a	$ \alpha^R ^2$ $\frac{4hc}{4\pi}$ ($10^{-13} \text{ cm}^{-1} \text{ esu}$)	Δ_{exp} (cm^{-1})	$\chi^{(3)E}$ (10^{-14} esu)
$\chi_{1111}^{(3)}$	530	13.5 (± 2)	25 \pm 1.5	1.80 \pm 0.08 (± 0.4)
	556		27.0 \pm 1.0	1.67 \pm 0.07 (± 0.3)
$\chi_{3333}^{(3)}$	530	2.7 (± 0.7)	8.6 \pm 0.7	1.0 (± 0.2)

the various components of the electronic nonlinear susceptibility tensor in terms of known Raman cross sections.

By varying the frequency ω_1 , keeping $\omega_1 - \omega_2$ fixed, the dispersion when $2\hbar\omega_1$ approaches two-photon resonances may be probed. This provides a sensitive and accurate calibration of such two-photon-absorption processes.

The directional properties of the complex tensor susceptibility $\chi^{(3)}$ are particularly sensitive to the presence of near-resonant contributions at combination frequencies such as $\omega_1 - \omega_2$ and $2\omega_1$. The phenomenon of dispersion of the plane of polarization at the combination frequency $2\omega_1 - \omega_2$ has been demonstrated.

The three-wave-mixing technique permits one to probe dispersive features in strongly absorbing spectral regions of the material, while the frequencies of the laser beams and the observed signal all lie in a transparent region of the spectrum. The

present study has shown the influence of vibrational resonances in the infrared and uv two-photon resonances, while the input and output beams used in the experiment all lie in the transparent region of the visible spectrum.

Simplified models for predicting features of the electronic nonlinearity $\chi^{(3)\epsilon}$ are useful to establish certain large scale qualitative trends. They are not able to forecast details of the spatial anisotropy, determined by the ratio of tensor elements, nor the detailed nonlinear frequency dispersion.

ACKNOWLEDGMENTS

The authors wish to acknowledge the loan of diamond samples by Dr. E. Anasstassakis, and the technical assistance of S. Maurici in preparing other crystalline samples. Shen Jen contributed valuable spontaneous Raman measurements, and A. J. Schell and N. M. Levenson assisted in taking and analyzing some of the data.

*Supported by Joint Services Electronics Program.

†Current Address: Physics Department, University of Southern California, Los Angeles, Calif. 90007.

- ¹N. Bloembergen, *Nonlinear Optics* (Benjamin, New York, 1965).
- ²P. D. Maker and R. W. Terhune, *Phys. Rev.* **137**, A801 (1965).
- ³E. Yablonovitch, N. Bloembergen, and J. J. Wynne, *Phys. Rev. B* **3**, 2060 (1971). See also F. DeMartini, F. Simoni, and E. Santamato, *Opt. Commun.* **9**, 176 (1973).
- ⁴Y. R. Shen, *Appl. Phys. Lett.* **23**, 516 (1973).
- ⁵M. D. Levenson, C. Flytzanis, and N. Bloembergen, *Phys. Rev. B* **6**, 3962 (1972).
- ⁶M. D. Levenson and N. Bloembergen, *J. Chem. Phys.* **60**, 1323 (1974).
- ⁷C. Flytzanis, Theory of Optical Nonlinear Susceptibilities, Harvard Univ., DEAP Report (unpublished); in *Treatise in Quantum Electronics*, edited by H. Rabin and C. L. Tang (Academic, New York, to be published).
- ⁸E. Yablonovitch, C. Flytzanis, and N. Bloembergen, *Phys. Rev. Lett.* **29**, 865 (1972).
- ⁹J. J. Wynne, *Phys. Rev. Lett.* **29**, 650 (1972).
- ¹⁰S. Kramer, F. Parsons, and N. Bloembergen, *Phys. Rev. B* **9**, 1853 (1974).
- ¹¹J. A. Armstrong, N. Bloembergen, J. Ducuing, and P. S. Pershan, *Phys. Rev.* **127**, 1918 (1962).
- ¹²B. F. Levine, *Phys. Rev. Lett.* **22**, 789 (1969); **25**, 440 (1970).
- ¹³C. C. Wang and N. W. Ressler, *Phys. Rev. B* **2**, 1827

(1970).

- ¹⁴N. Boling, A. Owyong, and A. J. Glass, *IEEE J. Quant. Elect.* (to be published).
- ¹⁵D. A. Kleinman, *Phys. Rev.* **126**, 1977 (1962).
- ¹⁶T. W. Hänsch, *Appl. Opt.* **11**, 895 (1972).
- ¹⁷J. T. Warden and Lucille Googh, *Appl. Phys. Lett.* **19**, 345 (1971). K. H. Drexhage, *Laser Focus* **9**, 35 (1973).
- ¹⁸E. Anasstassakis and E. Burstein, *Phys. Rev. B* **2**, 1952 (1970).
- ¹⁹M. D. Levenson, *IEEE J. Quant. Elect.* **QE-10**, 110 (1974).
- ²⁰J. G. Skinner and W. G. Nilsen, *J. Opt. Soc. Am.* **58**, 113 (1968).
- ²¹A. K. McQuillan, W. R. L. Clements, and B. P. Stoicheff, *Phys. Rev. A* **1**, 628 (1970).
- ²²V. S. Gorelik and M. M. Sushchinskii, *Fiz. Tverd. Tela* **12**, 1475 (1970) [*Sov. Phys. -Solid State* **12**, 1157 (1970)].
- ²³G. Bisson, G. Bret, M. Deniarietz, F. Gires, G. Mayer, and M. Paillette, *J. Chim. Phys.* **64**, 197 (1967).
- ²⁴C. D. Clarke, P. J. Dean, and P. V. Harris, *Proc. R. Soc. A* **277**, 312 (1964).
- ²⁵S. A. Solin and A. K. Ramdas, *Phys. Rev. B* **1**, 1687 (1970).
- ²⁶W. B. Lacina and P. S. Pershan, *Phys. Rev. B* **1**, 1765 (1970).
- ²⁷S. P. S. Porto, J. A. Giordmaine, and T. C. Damen, *Phys. Rev.* **147**, 608 (1966).

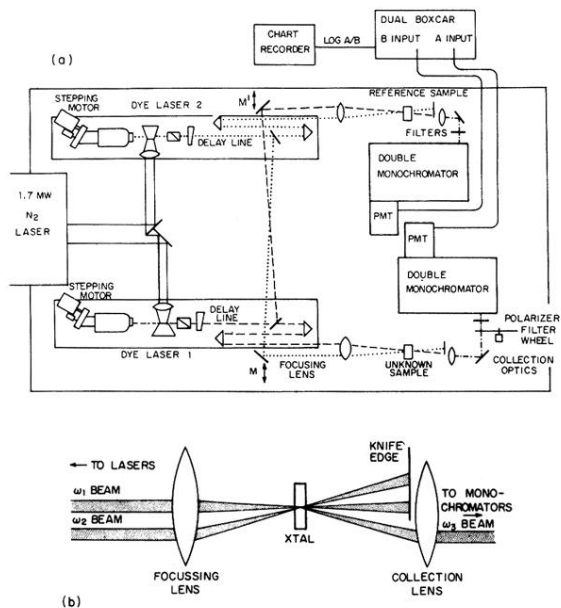


FIG. 3. (a) Experimental equipment employed in optical-mixing spectroscopy. The transversely moveable mirrors at M and M' allow independent adjustments of the crossing angle (and thus coherence length) in each arm of the experiment. (b) Detail of the sample region. Two laser beams are incident upon the crystal, and a third wave is generated by the cubic nonlinearity. The laser beams transmitted through the crystal are blocked, and the third wave is collected and imaged on the monochromator slit.